Interfacial spin-orbitronic effects controlled by different oxidation levels at the Co/Al interface

Sachin Krishnia,[1,*,†] Libor Vojáček,[2] Tristan da Câmara Santa Clara Gomes,[1,‡] Nicolas Sebe,[1] Fatima Ibrahim,[2] Jing Li,[3] Luis Moreno Vicente-Arche,[1] Sophie Collin,[1] Thibaud Denneulin,[4] Rafal E. Dunin-Borkowski,[4] Sergey A. Nikolaev,[5] Philippe Ohresser,[6] Nicolas Jaouen,[6] André Thiaville,[7] Albert Fert,[1] Henri Jaffrès,[1] Mairbek Chshiev,[2,8] Nicolas Reyren,[1] and Vincent Cros[1,§]

[1] *Laboratoire Albert Fert, CNRS, Thales, Université Paris-Saclay, 91767 Palaiseau, France*
[2] *Université Grenoble Alpes, CEA, CNRS, IRIG-SPINTEC, 38000 Grenoble, France*
[3] *Université Grenoble Alpes, CEA, Leti, 38000 Grenoble, France*
[4] *Ernst Ruska-Centre for Microscopy and Spectroscopy with Electrons (ER-C-1), Forschungszentrum Jülich GmbH, 52425 Jülich, Germany*
[5] *Osaka University, Toyonaka, Osaka 560-8531, Japan*
[6] *Synchrotron SOLEIL, L'Orme des Merisiers, 91190 Saint Aubin, France*
[7] *Laboratoire de Physique des Solides, Université Paris-Saclay, CNRS, Orsay 91405, France*
[8] *Institut Universitaire de France, 75231 Paris, France*

(Received 15 September 2024; revised 14 July 2025; accepted 16 July 2025; published 22 August 2025)

Perpendicular magnetic anisotropy (PMA) and Dzyaloshinskii-Moriya interactions are key interactions in modern spintronics. These interactions are thought to be dominated by the oxidation of the Co/Al interface in the archetypal platinum-cobalt-aluminum oxide system. However, in this study, we observe a double sign change in the anisotropy and about threefold variation in interfacial chiral interaction, influenced not only by the oxidation, but also by the metallic Al thickness. Contrary to previous assumptions about negligible spin-orbit effects at light metal interfaces, we observe not only strong PMA with fully oxidized Al, decreasing and turning negative (in-plane) with less oxygen at the Co/Al interface, but also that the magnetic anisotropy reverts to positive (out-of-plane) values at a fully metallic Co/Al interface. These findings suggest modification in the Co *d* band via Co/Al orbital hybridization, an effect supported by x-ray absorption spectroscopy and *ab initio* theory calculations, highlighting the key impact of strain on interfacial mechanisms at a fully metallic Co/Al interface.

DOI: 10.1103/gtwk-mq1y

I. INTRODUCTION

Breaking of inversion symmetry at interfaces together with the presence of a sizable spin-orbit coupling (SOC) are the two major components of a collection of phenomena in modern surface magnetism and spintronics [1]. These are interfacial effects, such as magnetic anisotropy [2], interfacial Dzyaloshinskii–Moriya interaction (i-DMI) [3,4], as well as charge-to-spin and charge-to-orbit interconversion mechanisms [5,6]. Early experiments in the 1990s considered bilayers of ferromagnet (FM) and heavy material films (or multilayers), an archetypal structure being Pt/Co bilayers, to exhibit large interfacial perpendicular magnetic anisotropy (PMA). In these systems, the large SOC of Pt combined with the orbital hybridization at the Pt/Co interface results in strong interfacial PMA [7–9].

Moreover, triggered by the search for a large room-temperature tunnel magnetoresistance effect in the 2000s, a large number of studies were then carried out on multilayered systems composed of a heavy material, e.g., Pt, a transition-metal magnetic material, e.g., Co, and an oxide, e.g., Al_2O_3 or MgO, showing large effective PMA [10–12]. Pioneer experiments on Pt/Co/AlO_x trilayers highlighted

*Contact author: sachinbudana@gmail.com
†Present address: Institute of Physics, Johannes Gutenberg University Mainz, Staudingerweg 7, 55128 Mainz, Germany.
‡Present address: INESC Microsistemas e Nanotecnologias (INESC MN) Rua Alves Redol 9, 1000-029 Lisbon, Portugal.
§Contact author: vincent.cros@cnrs-thales.fr

the necessity for optimum interface oxidation and established a paradigm for obtaining effective PMA [2,11,13,14]. In particular, it was shown that effective PMA drastically diminishes with slight over- or underoxidation of the Co/AlO_x interface, with a magnetization of Co that finally can be found in some cases to be in-plane even for 0.6-nm-thick Co films. Remarkably, in these experiments and in follow-up theoretical works, the interfacial anisotropy at the transition-metal/oxide interfaces was found to be of similar amplitude to that of the Co/Pt interface, despite the involvement of light elements with weak spin-orbit coupling, namely, Co, Al, and O [2,13]. The origin of the large PMA in optimum $Pt/Co/AlO_x$ structures has been associated with the hybridization between Co 3*d* and O 2*p* orbitals similar to the case of Co/MgO interfaces [11,15,16].

However, the underlying physical mechanism of PMA to in-plane effective anisotropy transition with underoxidation of the Co/AlO_x interface is still under debate after more than two decades. The recent prediction and observation of enhanced PMA at Co/graphene and Co/*h*-BN interfaces further challenges conventional understanding of the origin of these effects [17–21]. Recent results show that, with Al protected from oxidation, a purely metallic Co/Al interface exhibits an orbital texture which gives rise to efficient charge-to-orbit interconversion and very large enhancement of the current-induced torques on Co [6], as confirmed by *ab initio* calculations of orbital accumulation [22]. The present study aims to demonstrate that the richness of these interfaces is still surprisingly far from having been fully exploited, both from a physics point of view and for improving the performance of spintronic devices, offering a new paradigm of spin-orbit phenomena in them.

Another crucial interaction at play at the interface between a magnetic film and a light metal or an oxide film is the interfacial DMI that promotes the development of chiral magnetism and the associated different types of chiral spin textures, e.g., chiral domain walls, skyrmions, etc. [23]. Of interest for the present study, it has been shown that the $Pt/Co/AlO_x$ interface [24] exhibits one of the largest reported i-DMI values. However, the values measured on this system by various groups in the literature range from 0.5 to 2.5 pJ/m [25–28]. Therefore, it is also crucial to investigate how the i-DMI evolves with the oxidation degree of Al close to the interface and its microscopic origin in a $Pt/Co/(Al/)AlO_x$ multilayer. In this scenario, general questions arise about the physical mechanism through which the orbital hybridization between Al 3*p* and Co 3*d* orbitals impacts the effective PMA and DMI, and about the need to oxidize the Co/AlO_x interface to maximize the effects, which have been seen as a long-established requirement for more than two decades and have not yet been completely solved.

II. STRUCTURAL AND CHEMICAL CHARACTERIZATION OF Pt/Co/Al* MULTILAYERS

In this study, we thoroughly investigate the origin of several of these interfacial effects related to breaking of the inversion symmetry, orbital hybridization, and spin-orbit interaction at the model interface system, namely Pt/Co/Al*, where Al* refers to the natural oxidation of Al in air. By varying the deposited Al thickness, the Co/Al* interface termination is controlled to vary between Co—O—Al interface bonds, that is, an FM/oxide interface, and Co—Al interface bonds, that correspond to an FM/metal interface. The most striking result of our study is that the amplitude of the magnetic anisotropy strongly varies depending on the exact constitution of the interface.

Starting with a large perpendicular magnetic effective anisotropy at the $Co(0.9\ nm)/AlO_x$ interface (in agreement with previous works), it then rapidly decreases with increasing metallic Al and even undergoes a sign change. Importantly, we report that it experiences another sign change, overlooked until now, for thicker nominal Al, before it saturates upon the formation of a thicker metallic interface with stronger PMA. Such a double sign change of the effective anisotropy at the weak SOC Co/Al* interface suggests a mechanism involving orbital hybridization, which we verify by performing x-ray absorption spectroscopy (XAS) measurements combined with density-functional theory (DFT) calculations. In a correlated way, we find that the net i-DMI decreases with reduced oxygen atomic fraction at the Co/Al* interface, ultimately saturating for a fully metallic Co/Al interface, at a level of about one-third of the fully oxidized $Co(0.9\ nm)/Al*$ interface. It demonstrates again the strength of the DMI at the metallic Co/Al interface [29], which we find to be of similar magnitude as the one at the Pt/Co interface. These experimental results qualitatively match first-principles calculations in which the observed behavior is correlated with the interfacial dipole strength together with strain-induced effects.

Our approach is to fine-tune the oxygen content at the Co/Al* interface in a series of samples of composition $Si(sub.)/SiO_2(280\ nm)/Ta(5\ nm)/\ Pt(8\ nm)/Co(0.9\ nm)/Al*(t_{Al*})$, where the nominal thicknesses are given in parentheses. The absolute error on the thickness is evaluated to be below 0.1 nm, corresponding to the symbol size in the following figures. The samples are grown by dc magnetron sputtering onto thermally oxidized $Si/SiO_2(280\ nm)$ substrates. The 5-nm-thick Ta seed layer is introduced to ameliorate the adhesion and the surface roughness of the consecutive layers. It also results in an increase of PMA at the Pt/Co interface by improving the Pt texture [30]. The bilayer composed of 8 nm of Pt and 0.9 nm of Co is kept nominally the same in all the series. We only modulate the top Al layer with a systematic variation

in Al nominal thickness in steps of 0.1 nm. Note that it is well known that the bottom Pt/Co interface is the site of several interfacial effects related to inversion symmetry breaking and SOC, such as a large PMA identified in the 1990s [31], and, more recently, strong i-DMI observed since 2015 [24].

The main objective of this study is to investigate how the total effective magnetic anisotropy and the i-DMI are modified by adding, on top of Co, a film of a light element, namely Al, with different oxidation states on top of this model Pt/Co bilayer. With this aim, it is crucial to distinguish intrinsic effects related to electronic and orbital effects from extrinsic structural effects, such as interfacial intermixing [32], grain structure, or strain. Prior to focusing on the evolution of the anisotropy and i-DMI, we hence investigate both the chemical and structural nature of our samples, with a particular focus on the interface quality.

We first employ the scanning transmission electron microscopy (STEM) technique. In Fig. 1(a), we present a high-angle annular dark-field (HAADF) image of a Pt/Co/Al*(0.7 nm) sample together with the spatial distribution of the different elements, namely Pt (light gray), Co (blue), Al (green), and O (red) obtained using the energy-dispersive x-ray spectroscopy (EDX) technique [see Fig. 1(b)]. The STEM and EDX measurements demonstrate a very homogeneous polycrystalline growth of the different layers in the stack, as well as the existence of sharp interfaces between both Pt/Co and Co/Al*. From the STEM characterization together with a detailed x-ray diffraction (XRD) study, presented in Appendix A, we conclude that our Co films are growing mostly in the ϵ phase, that is, with hcp stacking.

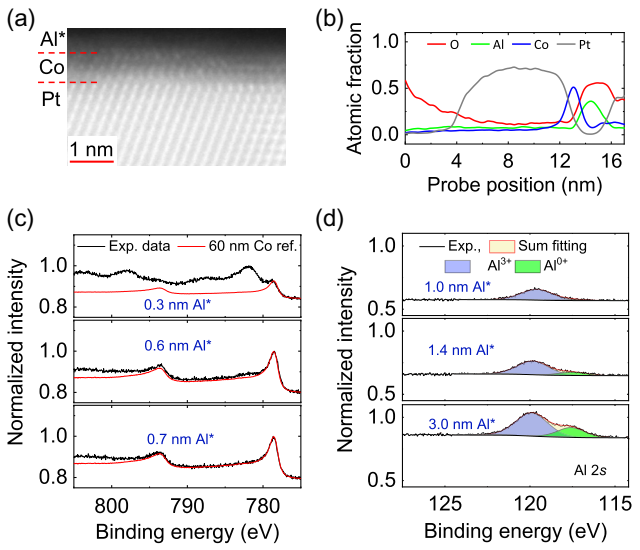

FIG. 1. Structural and chemical characterization of the multilayer. (a) HAADF STEM image showing the contrast of the Pt/Co/Al*(0.7 nm) sample. (b) Depth profile of integrated (over 30 nm) atomic fraction of Pt (light gray), Co (blue), Al (green), and O (red) along the thickness. (c) XPS spectra (black) near the Co $2p$ energy from Pt/Co/Al*(t_{Al*}) for $t_{Al*} = 0.3$, 0.6, and 0.7 nm, with a reference spectrum of *in-situ*-grown 60-nm Co (red). (d) XPS spectra (black) near the Al $2s$ energy from Pt/Co/Al*(t_{Al*}) for $t_{Al*} = 1.0$, 1.4, and 3 nm. Fitted peaks of Al^{3+} and Al^0 are shown by blue and green envelopes, while the total areas are filled with light yellow.

To access more precisely the oxidation states of Co and Al atoms in the Pt/Co/Al*(t_{Al*}) series, we perform x-ray photoelectron spectroscopy (XPS) experiments on samples with various t_{Al*}. In Fig. 1(c), we present the XPS spectra (black curves) collected at Co $2p$ levels for three different thickness of Al*, namely 0.3, 0.6, and 0.7 nm. In addition, we also include in Fig. 1(c) (red curves) the XPS spectra measured on an *in-situ*-grown 60-nm thick Co film considered as a reference for metallic Co. We clearly see that the spectrum for $t_{Al*} = 0.3$ nm is very different from that of the reference Co, indicating the partial oxidation of Co with two peaks at 778.6 and 781.9 eV corresponding to Co $2p_{3/2}$ and CoO $2p_{3/2}$, respectively. The CoO $2p_{3/2}$ peak at 781.9 eV is strongly decreased for $t_{Al*} = 0.6$ nm, and has even completely disappeared for $t_{Al*} = 0.7$ nm. In consequence, we conclude from these XPS characterizations that 0.7 nm of Al* is thick enough to completely protect Co from oxidation (at least over the several months of the experiments). In the following, samples with Al* thickness thinner than this threshold value will not be considered.

Important complementary information is to determine the presence of either metallic or oxidized Al at the Co/Al* interface. Therefore, we also measured the XPS spectra at the Al $2s$ edge for several t_{Al*}, as shown in Fig. 1(d). The spectra obtained for $t_{Al*} \leq 1$ nm reveal solely the Al^{3+} valence state, consistent with a full oxidization of the Al film. Above 1 nm, the Co/Al* interface starts to display a metallic character, as demonstrated by the presence of a peak associated with metallic Al (Al^0). Finally, we emphasize that the conclusions obtained from the analysis of the XPS measurements are quantitatively consistent with those from x-ray absorption spectroscopy shown in Appendix B.

III. SPIN AND ORBITAL MOMENTS AND i-DMI IN Pt/Co/Al* MULTILAYERS

Next, we quantitatively determine the spin (S_z) and orbital (L_z) moments of Co using x-ray absorption spectroscopy and x-ray magnetic circular dichroism (XMCD) at the Co $L_{2,3}$ edges. In Fig. 2(a), we display the mean XAS and the XMCD spectra for two samples with different t_{Al*} thickness, namely 0.7 and 2 nm. For 0.7 nm, the case of absence of Co oxidation and full oxidization of the Al film according to XPS, the shapes of both the XAS and XMCD spectra are typical of those recorded for bulk Co [33]. Applying the XMCD sum rules, we find $S_z = 1.8\ \mu_B$/atom, which is about 15% higher than the value for bulk Co. For $t_{Al*} = 2$ nm, the existence of

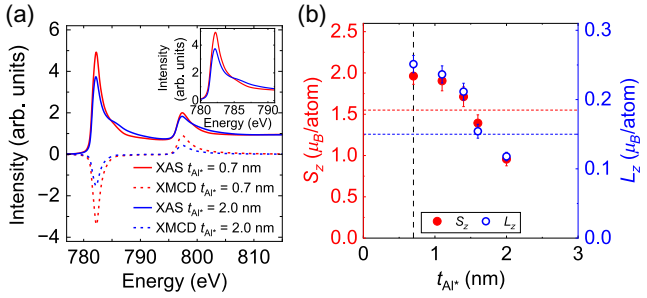

FIG. 2. (a) XAS and XMCD spectra from the Co L_3 and L_2 edges in Pt/Co/Al* for $t_{Al*} = 0.7$ nm (red) and 2.0 nm (blue) at room temperature. The inset shows an enlargement of the XAS spectra around the L_3 edge. (b) Spin and orbital magnetic moments of Co atoms as a function of Al* thickness estimated from sum rules. The vertical dashed line corresponds to $t_{Al*} = 0.7$ nm, which is the minimum Co thickness for ensuring nonoxidized Co. The two horizontal dotted lines indicate the spin and orbital moments for bulk Co (from Ref. [33]).

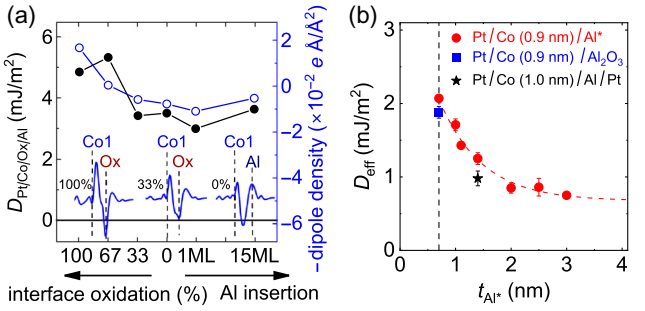

FIG. 3. DMI modulation with the oxidation level at the Co/Al* interface. (a) Effective DMI coefficient of Pt/Co/(Ox)Al_2O_3 calculated from the *ab initio* total-energy method. Its decrease is correlated to the Co/Ox interfacial dipole (Rashba-type DMI) formed by charge transfer to the oxygen as shown in insets for 100%, 33%, and 0% O content at the interface. (b) Experimental variation in effective DMI measured by Brillouin light scattering, as a function of t_{Al*} (red). The DMI values from other studies in the case of oxide (Pt/Co/Al_2O_3) [24] and metallic (Pt/Co/Al/Pt) [29] top interfaces are also displayed by a blue square and a black star, respectively. Assuming an i-DMI independent of the Co thickness, the Pt/Co(0.9 nm)/Al point can be calculated (black star).

Co—Al bonds associated with the presence of a nonoxidized Al film result in some noticeable changes of the XAS spectra at both L_3 and L_2 edges [see Fig. 2(a)], notably with a strong drop of peak intensity associated with a large variation in the number of unoccupied Co d states as well as the appearance of a shoulder peak after the L_3 edge. This latter reflects a significant change in the Co band structure in the case of the Co/Al interface.

In Fig. 2(b), we present how the transition from Co—O—Al bonds to Co—Al impacts both the evolution of spin (S_z) and orbital (L_z) Co magnetic moments when t_{Al*} increases. Both S_z and L_z remain slightly higher than bulk Co values up to $t_{Al*} = 1.4$ nm before they both continuously drop, reaching an S_z value of 1 μ_B/atom for $t_{Al*} = 2$ nm. The observed evolution of the magnetic moments with Al* thickness has been confirmed by SQUID magnetometry (see Appendix C).

To understand the microscopic origin of the evolution of Co spin and orbital moments with t_{Al*}, but also, as described later, of i-DMI and the anisotropy, we have performed *ab initio* calculations within density-functional theory with the Perdew-Burke-Ernzerhof functional (DFT/PBE) [34,35] as implemented in the Vienna *Ab initio* Simulation Package (VASP) [36–39]. For that, we have constructed a heterostructure of a four-monolayer hcp(0001) Co film and α-Al_2O_3 with varying interface oxidation and Al insertion in between. Details on the DFT methodology, the simulated structures [both hcp(001) and fcc(111)] Co, as well as the calculations of spin and orbital magnetic moments are presented in Appendixes E, F, and J. The experimental results shown in Fig. 2 are found to be in good quantitative agreement with the DFT ones for hcp(001) Co. First, we note that the large S_z for $t_{Al*} = 0.7$ nm is attributed mainly to a higher S_z for the Co atoms at the interface with the oxide, similarly to what was found at a Co/MgO interface [15]. Second, we find that, as the Co/Al* interface becomes metallic with increasing Al* thickness, the interfacial Co acquires a negative charge, leading to a reduced magnetic moment of about 20%.

In Fig. 3(a), we present the DFT results for the evolution of the i-DMI constant obtained from the energy difference between the clockwise and counterclockwise spin configurations [15]. To compare with the experimental values, several Co/Al* structures have been constructed in which the oxygen is gradually removed from the interface (see Appendix E for visualization of the structures).

In Fig. 3(b), we display how the effective DMI D_{eff} amplitude measured by Brillouin light scattering (BLS) spectroscopy evolves as a function of the Al* thickness. The large DMI value measured for $t_{Al*} = 0.7$ nm, close to 2 mJ/m^2, is found to closely match that measured by Belmeguenai *et al.* [24], where they deposited an oxide layer on top of the Co (i.e., Pt/Co/Al_2O_3) [blue square in Fig. 3(b)]. Then, with increasing t_{Al*}, D_{eff} exhibits an exponential-like decay, saturating for $t_{Al*} \gtrsim 2$ nm (decay length is about 1.3 nm). For $t_{Al*} = 1.4$ nm, the measured DMI is very close to that in the fully metallic Al case when capped by Pt, which was measured by BLS in Ta(5 nm)/Pt(8 nm)/Co(1.0 nm)/Al(1.4 nm)/Pt(3 m) in a previous study [29] [black star in Fig. 3(b)]. Note that this last value is slightly smaller, but once the DMI value is renormalized by the Co thickness, assuming that the DMI can be written as $D_{eff} = D_s/t_{Co}$ (D_s is the i-DMI interfacial energy), we find the star, which coincides with our data for $t_{Al*} = 1.4$ nm. Given that the bottom Pt/Co interface is identical in all samples, and considering the weak

expected SOC at the top Co/Al* interface, the experimental decrease in D_{eff} with $t_{\text{Al*}}$ is attributed to the variation in the electronic filling of the Co d band at the Co/Al* interface, which depends on the thickness of $t_{\text{Al*}}$, as revealed by our XAS and XMCD measurements (Fig. 2).

Interestingly, we find that the observed trend is reproduced by the *ab initio* calculations [black curve in Fig. 3(a)], with a decreasing tendency when oxygen is removed from the Co/Al_2O_3 interface. This behaviour is explained by electron transfer from Co to nearby O atoms, which is stronger for larger oxidation, and which creates an interfacial charge dipole [blue curve in Fig. 3(a)]. This electric dipole induces a Rashba-type DMI [40,41] at the Co/Al* interface, which is additive to the DMI contribution from the bottom Pt/Co (see Appendixes D, G, and H for details of the BLS experiments and *ab initio* DMI calculation).

IV. DOUBLE SIGN CHANGE OF MAGNETIC ANISOTROPY WITH Al* THICKNESS

Another striking result of the present study is the strong and unexpected Al thickness dependence of the magnetic anisotropy in the Pt/Co/Al* system, which was used about two decades ago for optimizing the perpendicular anisotropy [2,11,13]. In Fig. 4, we present experimental measurements of the out-of-plane effective anisotropy field ($\mu_0 H_K$) versus Al* thickness. The effective anisotropy has been determined through the anomalous Hall effect, measuring the transverse resistance (R_{xy}) as a function of in-plane and out-of-plane magnetic fields, on 5-μm-wide Hall bars. In the inset of Fig. 4 are plotted several normalized R_{xy} curves as a function of out-of-plane magnetic field (H_z) in Pt/Co/Al*($t_{\text{Al*}}$) samples for a few relevant $t_{\text{Al*}}$ values.

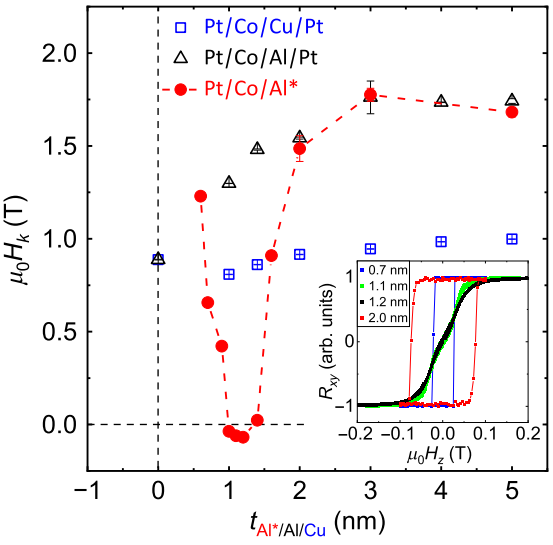

FIG. 4. Out-of-plane effective anisotropy field as a function of Al* (red), Al (black), and Cu (blue) thicknesses in Pt/Co/Al*($t_{\text{Al*}}$), Pt/Co/Al(t_{Al})/Pt, and Pt/Co/Cu(t_{Cu})/Pt samples. The inset shows the normalized transverse resistance R_{xy} as a function of the out-of-plane magnetic field in Pt/Co/Al*($t_{\text{Al*}}$) for $t_{\text{Al*}} = 0.7, 1.1, 1.2, 2.0$ nm.

As demonstrated above by XPS measurements (Fig. 1), the Co remains nonoxidized for $t_{\text{Al*}} = 0.7$ nm, resulting in a square hysteresis loop with sharp magnetization reversal and finite coercive field, confirming a large PMA (about ≈ 1.2 T), in quantitative agreement with previous results [2,11]. Upon increasing the Al* thickness to 1.1 nm, the positive $\mu_0 H_K$ drops rapidly and Co magnetization turns in-plane ($\mu_0 H_K$ reaching a negative value of about -70 mT), as shown by green and black loops in the inset for $t_{\text{Al*}} = 1.1$ and 1.2 nm, respectively. The anisotropy is found to be negative for $t_{\text{Al*}}$ between 1.0 and 1.4 nm. It is worth recalling that the XPS data confirm the presence of metallic Al at the Co/Al* interface for $t_{\text{Al*}} \geq 1.1$ nm. For $t_{\text{Al*}} = 1.4$ nm, $\mu_0 H_K$ is found to be $+23$ mT, at the verge of the second sign change. At larger $t_{\text{Al*}}$, the anisotropy continues to increase until it saturates at about 1.8 T for $t_{\text{Al*}} \geq 2$ nm (see the square loop for $t_{\text{Al*}} = 2.0$ nm in the inset of Fig. 4).

In Fig. 4, we also include in some points of anisotropy values obtained from two other Pt/Co-based metallic systems, namely Pt/Co(0.9 nm)/Cu(t_{Cu})/Pt(3 nm) (open blue square) and Pt/Co(0.9 nm)/Al(t_{Al})/Pt(3 nm) (open black triangle). Importantly, in these two systems, the presence of a 3-nm-thick Pt cap layer completely prevents the light element becoming oxidized [6]. For Pt/Co/Cu(t_{Cu})/Pt, we find that $\mu_0 H_K$ remains almost constant with Cu thickness (blue open squares in Fig. 4) akin to the symmetric Pt/Co/Pt structure for $t_{\text{Cu}} = 0$ (0.9 T). In contrast, the anisotropy in the Pt/Co/Al(t_{Al})/Pt series (black open triangles in Fig. 4) exhibits an increase with Al thickness, saturating at 1.8 T for $t_{\text{Al}} = 3$ nm. An interesting observation is that, for t_{Al} larger than 2 nm, the measured anisotropies exactly (within error margins) correspond to the values measured in the Pt/Co/Al* systems, in which a metallic Al film is present. The twofold enhancement in anisotropy found in Pt/Co/Al* (and also in Pt/Co/Al/Pt) compared to Pt/Co/Cu/Pt and the symmetric Pt/Co/Pt structure underscores the substantial role of the metallic Co/Al interface on interfacial properties.

In order to get insights about the physical origin of these observations, we have performed *ab initio* calculations of magnetic anisotropy energy [42] and found in the case of Co hcp(001) the same decrease and subsequent enhancement of PMA as observed in the experiments [see Fig. 5(a)]. The PMA first decreases as the interfacial oxygen is progressively removed, turning down the hybridization between O p_z and Co d_{z^2} interfacial states. Interestingly, the calculations then suggest a strong PMA enhancement in the bulklike Co layers due to an in-plane tensile strain imposed on Co by the metallic Co/Al interface, as shown in Figs. 5(a) and 5(c). This large PMA

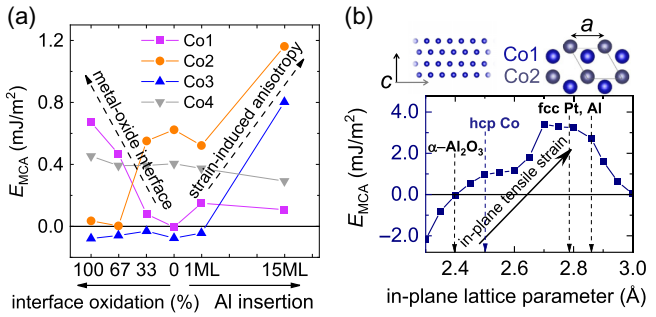

FIG. 5. Magnetocrystalline anisotropy energy E_{MCA} calculated from *ab initio* total energies in Co layers (Co1 is at the interface) as a function of (a) interfacial oxygen content and (b) in-plane lattice parameter. The vertical dashed lines in panel (b) indicate in-plane lattice parameters.

enhancement in the ultrathin Co film with an increasing lattice parameter is due to the increased density of states (DOS) of the in-plane ($d_{xy}, d_{x^2-y^2}$) minority electrons as the Co atoms get further apart. More results are presented in Appendixes G, H and J, in which the full discussion of the PMA calculations and the second-order perturbation theory analysis are provided, linking the PMA trends to electronic states with a specific orbital character. The results of DFT calculations for fcc(111) Co are also discussed. The general U-shaped trend of the calculated PMA matches well the experimentally observed one. In more detail, from the calculations, it appears that the PMA reduces up to about 1.0 nm before increasing again, while the experimental curve displays a PMA regain at about 1.4 nm. This should not be a surprise, as the calculations ignore the important, but *a priori* constant, role of the bottom Pt/Co interface.

V. CONCLUSION

In conclusion, our investigation into the Pt/Co/Al* model spintronic system elucidates the critical role of the Co/Al* interface on i-DMI and PMA. First, we establish a clear correlation between the reduction in oxygen concentration at the Co/Al* interface and a subsequent decrease in the net DMI, addressing discrepancies in measured values by different groups. Second, we observe a sign change in anisotropy indicating a transition from out-of-plane to in-plane orientation, at approximately a single aluminum metallic monolayer at the Co interface. Notably, the anisotropy of the Co layer undergoes a second sign change, and then saturates with the formation of a thick metallic interface characterized by enhanced PMA due to strong orbital hybridization at the Co/Al interface as revealed by XAS and DFT. Our experimental results reveal a new way to tune the interfacial properties with light metal interface, notably the i-DMI and PMA [43], for manipulation of the next generation of spinorbitronic systems.

ACKNOWLEDGMENTS

The authors acknowledge Yanis Sassi for fruitful advice and discussion. This work has been supported by a France 2030 Government grant managed by the French National Research Agency (ANR) PEPR SPIN CHIREX (Grant No. ANR-22-EXSP-0002), SPINMAT (Grant No. ANR-22-EXSP-0007), and SPINTHEORY (Grant No. ANR-22-EXSP-0009), by the ANR with TOPO3D (Grant No. ANR-22-CE92-0082) and by the European Horizon Europe Framework Programme under Grant No. 101135729 (SkyANN). This work contains results obtained from the experiments performed at the Ernst Ruska-Centre (ER-C) for Microscopy and Spectroscopy with Electrons at the Forschungszentrum Jülich (FZJ) in Germany. The ER-C beam-time access was provided via the DFG Core Facility Project ER-C E-014. This project has received funding from the European Union's Horizon 2020 Research and Innovation Program under Grant Agreement No. 800945 (NUMERICS–H2020-MSCA-COFUND-2017).

DATA AVAILABILITY

The data are not publicly available. The data are available from the authors upon reasonable request.

APPENDIX A: CHARACTERIZATION BY TEM AND EDX

For TEM and EDX, the cross-section lamella was prepared using a focused ion beam machine with a final thinning step at 8 kV. The surface of the sample was protected by a Pt layer deposited using electron-beam-induced deposition. In Fig. 6(a), we present a low-magnification HAADF image of the Pt/Co/Al*(0.7 nm) sample, which constitutes a Co/oxide interface. The HAADF image clearly reveals the polycrystalline nature of the Pt and Co layers and highlights the high interface quality of our samples. The average grain size in our sample can be estimated to be 4–5 nm. The (111) texture of the Pt layer is also suggested by the planes about parallel to the interface, and confirmed by x-ray diffraction (see Appendix I). The spatial distribution of Pt (light gray), Co (blue), Al (green), and O (red) obtained using the energy-dispersive x-ray spectroscopy technique is shown in Fig. 6(b). The elemental intensity along the sample thickness is plotted in Fig. 6(c). The STEM and EDX measurements reveal very homogeneous growth and sharp interfaces in our samples.

APPENDIX B: X-RAY ABSORPTION SPECTROSCOPY

In Fig. 7(a), we display the mean XAS spectra for samples with 0.5 and 0.7 nm Al* capping layers in the Pt/Co/Al*(t_{Al*}) series. The XAS and XMCD measurements are performed at the DEIMOS beamline at the

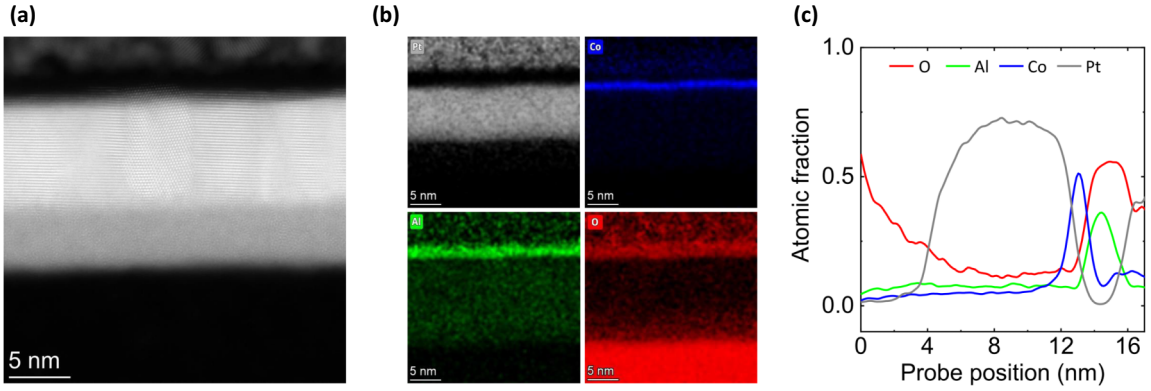

FIG. 6. (a) HAADF image of the Pt/Co/Al*(0.7 nm) sample. (b) EDX element mapping displaying the spatial distribution of Pt (light gray), Co (blue), Al (green), and O(red). (c) Depth profile of integrated atomic fraction of Pt, Al, Co, and O elements along the thickness.

SOLEIL synchrotron [44]. An enlargement of the XAS spectra is shown for comparison in Fig. 7(b). The pre-edge and post-edge intensities in the vicinity of 780.8 and 783.3 eV energies, respectively, are highlighted by blue dashed ellipses. In metallic Co, the pre-edge and post-edge regions are expected to be relatively smooth, with no significant peaks due to the absence of allowed transitions. However, in the presence of oxidized Co, the XAS spectrum in these regions exhibits small peaks or shoulders, attributed to quadrupole transitions or crystal-field effects, as indicated by the blue ellipses. The presence of pre-edge and post-edge shoulders in the sample with a 0.5 nm Al* capping layer hence suggests oxidation of Co. On the contrary, the sample with a 0.7 nm Al* capping layer shows no evidence of Co oxidation, which is consistent with our XPS measurements.

APPENDIX C: EXPERIMENTAL MAGNETIZATION AND ANISOTROPY

In Fig. 8(b), the interfacial anisotropy is calculated based on the polynomial fit (dashed line) of the spontaneous magnetization as measured by a superconducting quantum interference device (SQUID) [Fig. 8(a)]. For this estimation, we suppose that the effective anisotropy field can be written as $K_{u,s} = (\mu_0/2)M_s(M_s + H_K)t_{Co}$ using a fixed $t_{Co} = 0.9$ nm. The values can be compared to the *ab initio* ones detailed in Appendix H.

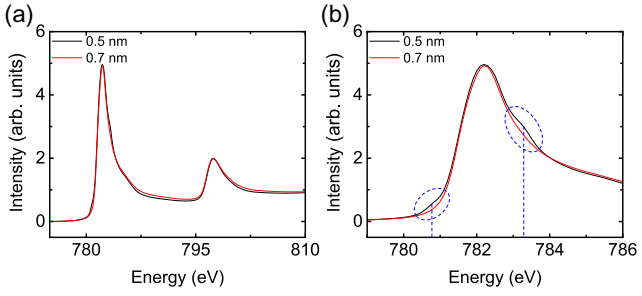

FIG. 7. (a) XAS spectra in the vicinity of the Co L_3 and L_2 edges in Pt/Co/Al*(t_{Al*}) for $t_{Al*} = 0.5$ nm (black) and 0.7 nm (red) at room temperature. (b) Enlarged image of panel (a) around the L_3 edge. The pre-edge (780.8 eV) and post-edge (783.3 eV) intensities of XAS are highlighted by dashed ellipses for comparison.

APPENDIX D: BRILLOUIN LIGHT SCATTERING

We performed spin-wave spectroscopy experiments using the Brillouin light-scattering (BLS) technique in Damon–Eshbach geometry to quantify the strength of DMI [24,45]. We probed Stokes (f_S) and anti-Stokes (f_{AS}) resonant frequencies using a green laser ($\lambda = 532$ nm), which correspond to counterpropagating spin waves transverse to the magnetization direction. The variation in the frequency difference ($\Delta f = f_{AS} - f_S$) with the incident wave vector

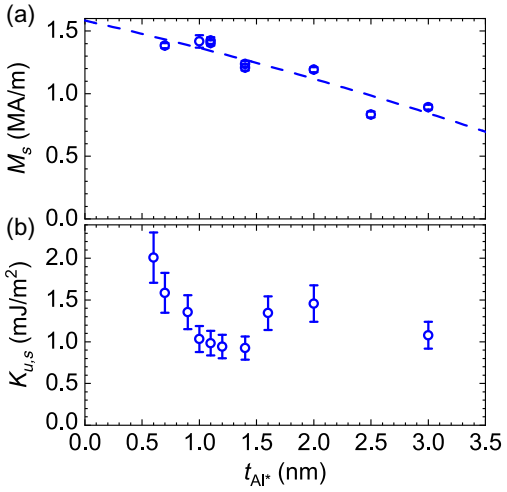

FIG. 8. Magnetometry. (a) Spontaneous magnetization (M_s) as a function of t_{Al*} in Pt/Co/Al*(t_{Al*}) samples. The M_s value is measured using SQUID and fitted by a parabola (dashed line). (b) Estimation of the uniaxial interfacial anisotropy (see text).

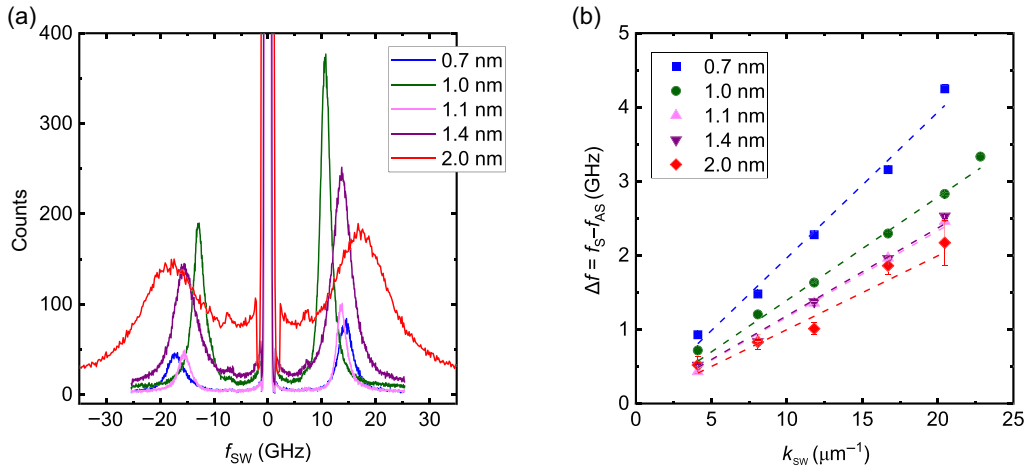

FIG. 9. (a) BLS spectra of Pt/Co/Al*(t_{Al*}) for various Al* thicknesses, obtained with a laser of wavelength 532 nm for $k_{sw} = 16.7\ \mu m^{-1}$. (b) DMI-induced frequency shifts of counterpropagating spin waves as a function of k_{sw}, measured in the Pt/Co/Al*(t_{Al*}) samples with different t_{Al*} equal to 0.6, 1.0, 1.4, and 2.0 nm. The dashed lines are linear fits.

(k_{sw}) is related to the effective DMI parameter (D_{eff}) as [24,45]:

$$\Delta f = -\frac{2\gamma}{\pi M_s} D_{eff} k_{sw}. \tag{D1}$$

Here, γ is the gyromagnetic ratio and M_s is the saturation magnetization of Co. To estimate D_{eff}, the magnetization of the Co layer is driven in-plane by applying large external magnetic fields while measuring the spin-wave dispersion as shown in Fig. 9(a), measured for various t_{Al*} in Pt/Co/Al*(t_{Al*}) samples. The change in Δf as a function of incident k_{sw} is shown in Fig. 9(b) for several samples. In accordance with Eq. (D1), Δf exhibits a linear dependence on k_{sw}. The D_{eff} for each sample is subsequently determined through a linear fit to the experimental data based on Eq. (D1).

APPENDIX E: *AB INITIO* CALCULATED STRUCTURES

Following the expected evolution of the experimental samples, we construct a heterostructure by interfacing a four-monolayer hcp(0001) Co slab and α-Al_2O_3, with hydrogen passivation on the oxygen-terminated free surface [46]. The crystalline Al_2O_3 emulates the usually amorphous AlO_x. The oxygen at the Co/Al_2O_3 interface is then gradually removed (with the interface oxidation represented in percentages) and the Al layer is inserted. We thus arrive at a progression of six structures, plotted in Fig. 10.

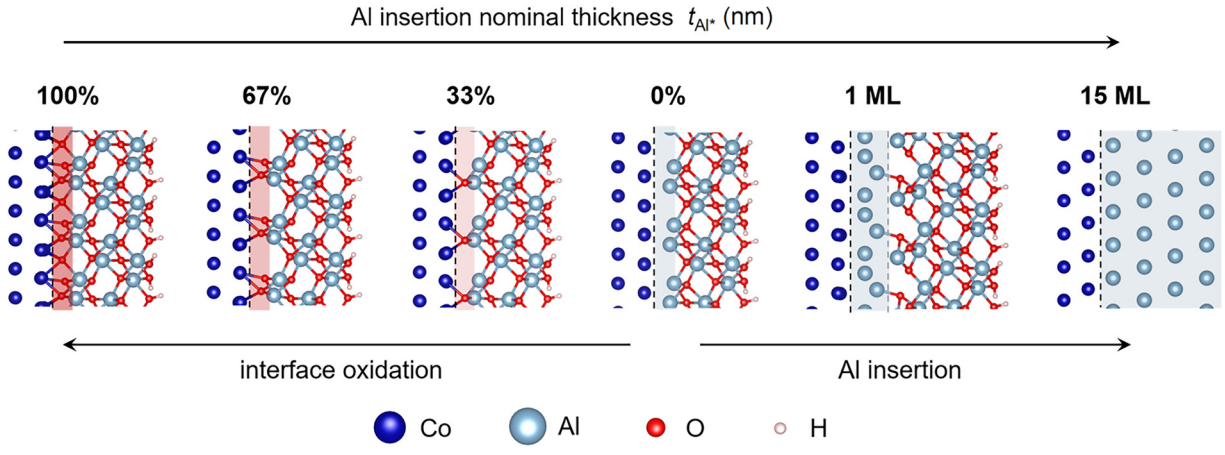

FIG. 10. The Co/Al/Al_2O_3 bilayers used to emulate the experimental evolution of a Co/Al/AlO_x bilayer with increasing Al insertion thickness. After the initial oxygen removal, the number of interfacial Al layers is increased. This corresponds to the experimental trend. Note that, in the interest of space, only two monolayers (ML) of Co are shown, instead of the full four-monolayer slab used in the calculations. This has been plotted with VESTA [47].

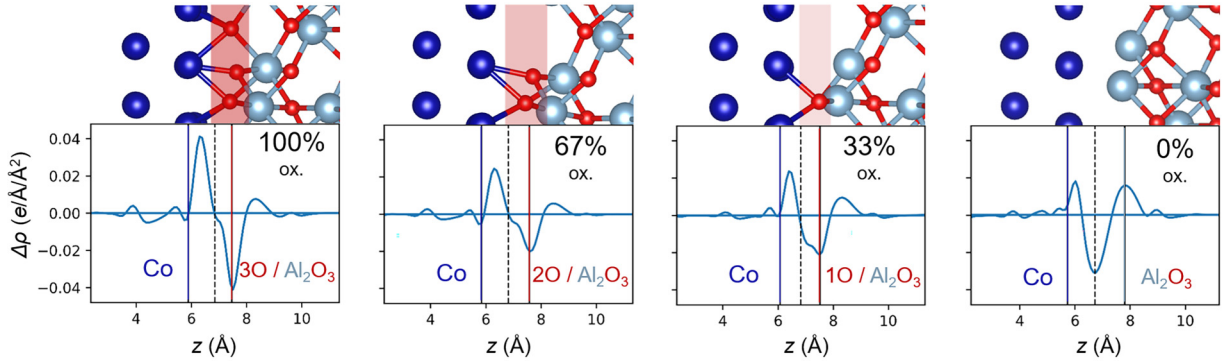

FIG. 11. The Co/Al_2O_3 interfacial charge dipole disappears with oxygen removal.

These structures were used for the *ab initio* calculations in this work.

APPENDIX F: *AB INITIO* METHODS

The *ab initio* calculations have been performed within DFT/PBE [34,35] as implemented in the VASP package [36–39]. During structural relaxations with the in-plane lattice parameter fixed, the forces were minimized below 1 meV/Å. The DMI constant is computed from the energy difference between the clockwise and counterclockwise spin configurations [48]. The magnetic anisotropy is obtained from the energy difference between the in-plane and out-of-plane-magnetized systems [42] and analyzed within second-order perturbation theory [49–51].

The Brillouin zone is sampled by a 15×15 Gamma-centered mesh, increased to 19×19 for the anisotropy and the DMI calculations. The plane-wave basis is expanded up to the cutoff energy of 500 eV. A vacuum spacer of ≈ 20 Å decoupled the bilayer from its periodic image in the out-of-plane direction. The four-monolayer (4 ML) Co slab in hcp(0001) ABAB stacking is found to be slightly (≈ 6 meV/Co atom) more stable than the fcc(111) surface with its ABCA stacking, as tested on a Co(4 ML)/Al(15 ML)

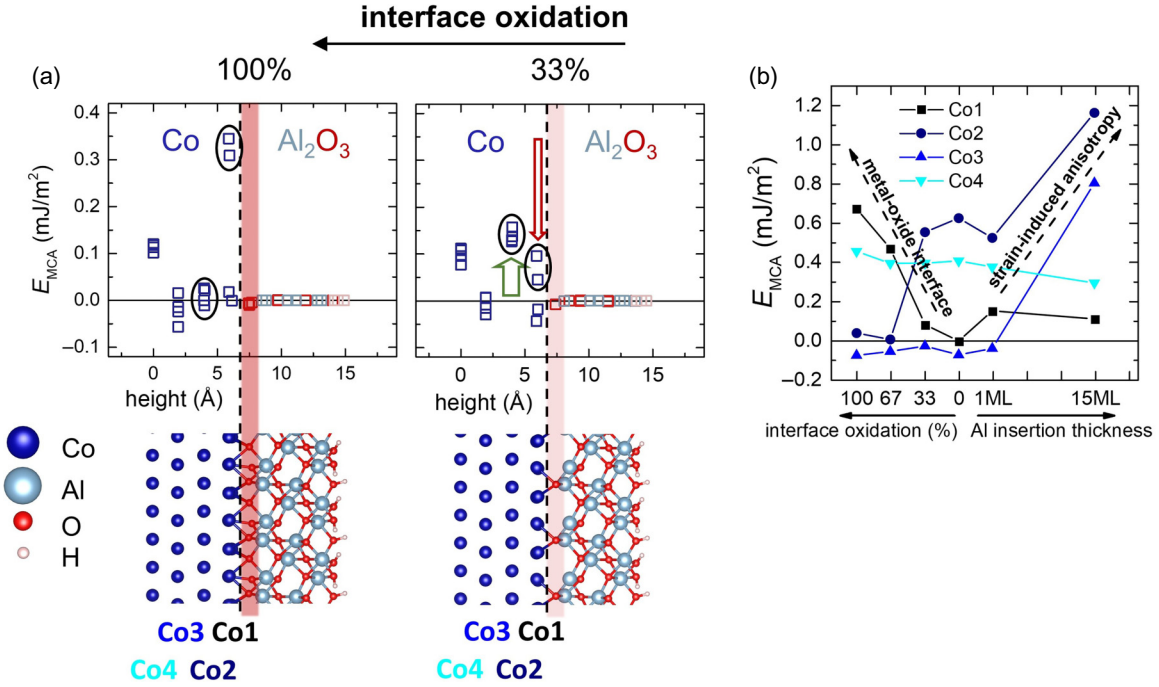

FIG. 12. (a) Layer-resolved PMA for 100% and 33% oxidized interface. Oxygen removal kills the PMA of the Co1 interfacial layer. Consequent Al insertion enhances PMA in the Co2 and Co3 bulklike layers via in-plane biaxial strain. (b) Layer-resolved PMA for all the structures shows these trends clearly. High PMA is obtained for the Co/Al_2O_3 interface with high oxygen content on one side (typical metal-oxide PMA [2]) and high aluminum content on the other side (strain-induced), with a dip in between these two extremes, where neither of the effects dominates.

bilayer with $a = 2.403$ Å. The in-plane lattice parameter is either $d_{Co–Co} = 2.4$ Å, corresponding to Al_2O_3 substrate, or $d_{Co–Co} = 2.86$ Å, corresponding to Al substrate, compared to the relaxed lattice parameter of hcp Co, $d_{Co–Co} = 2.5$ Å.

APPENDIX G: RASHBA-TYPE DMI AND INTERFACIAL DIPOLE

The variation of DMI with Al insertion is explained by the decreasing oxidation of the Co/Al_2O_3 interface: with oxygen present, a charge dipole is formed, giving rise to a Rashba-type DMI [40,41]. After oxygen removal, this charge dipole disappears in favor of a symmetrical metallic bond. The *ab initio* charge transfer due to the interface formation is shown in Fig. 11. Removing oxygen from the interface reduces the charge dipole until it completely vanishes for Co/Al.

APPENDIX H: PMA BEHAVIOR WITH OXIDATION AND STRAIN

The layer-resolved E_{MCA} values are shown in Fig. 12 and show the same drop and subsequent increase of PMA as the experimental data in Figs. 4 and 8. The decreasing and increasing trends in the PMA are attributed to two distinct phenomena.

First, from the layer-resolved anisotropy values in Fig. 12(a), it appears clearly that the interfacial Co1 layer loses its strong out-of-plane anisotropy after oxygen removal. This will be ascribed to O p_z and Co d_{z^2} hybridization in the perturbation analysis below.

Second, with continuing Al insertion, PMA is boosted in the bulklike Co2 and Co3 layers [Fig. 12(b)]. This can be attributed to strain-induced anisotropy: Co is expected to expand in-plane due to the lattice matching with Al. In Fig. 5(b), we demonstrate that in-plane biaxial strain indeed causes a large PMA increase in the four-monolayer

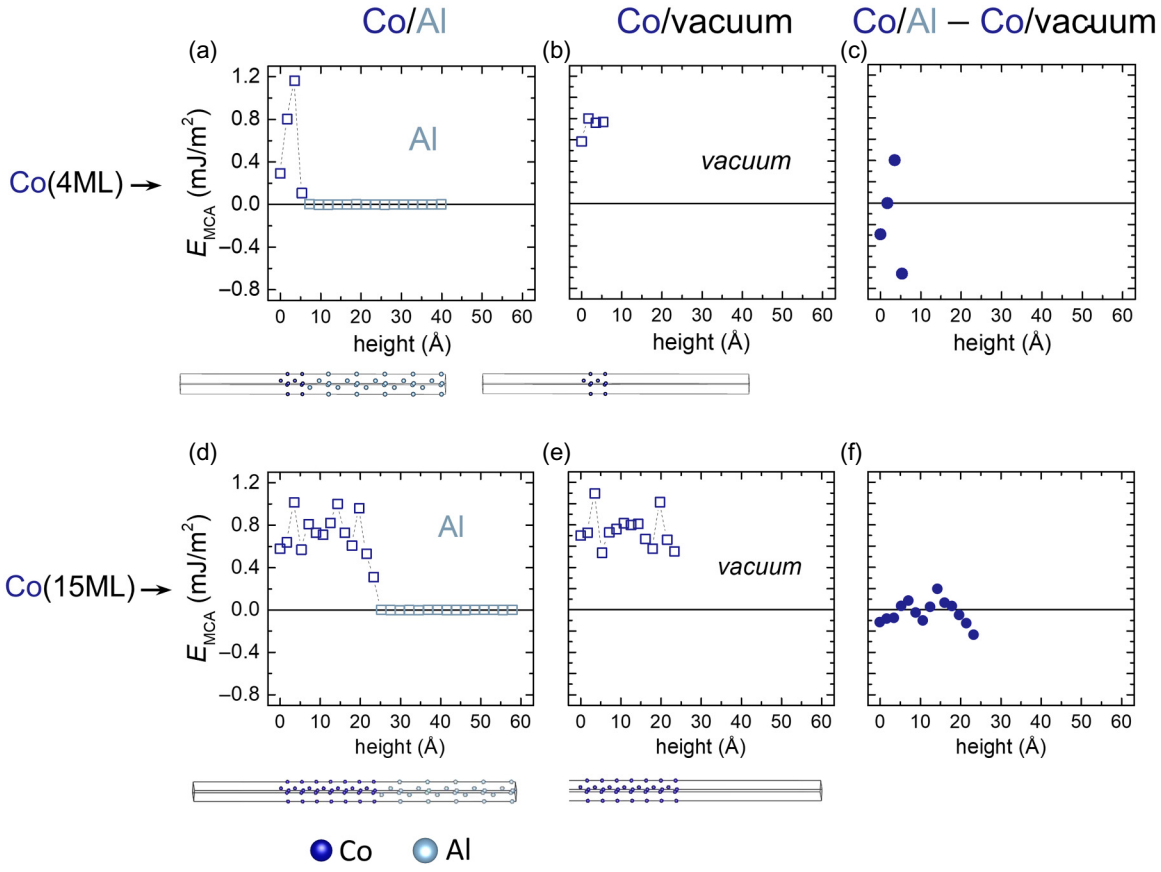

FIG. 13. Disentangling the Al strain and interface effects on the layer-resolved magnetocrystalline anisotropy (MCA) of Co. In panels (a) and (c) we consider the 4-ML-thick Co as used in the rest of the calculations in this work, while in panels (d) and (f) we consider a thicker (15-ML) Co film to better show the difference between the bulk and interfacial Co layers. The Al layer of the Co/Al bilayer in panels (a) and (d) is artificially removed in panels (b) and (e) while the Co structure is kept frozen (no relaxation performed after the Al removal). The difference of E_{MCA} between these two cases, shown in panels (c) and (f), emphasizes purely the effect of the Co/Al interface. It is clear from panels (b) and (d) that the PMA persists even without the presence of Al, hence the large bulklike PMA is mainly a structural effect. In fact, the role of the Al at the interface is rather to *decrease* the PMA of the interfacial Co layer, as clearly shown in panels (c) and (f).

hcp Co film. This will be traced back to the decrease in the width of d_{xy} and $d_{x^2-y^2}$ bands in the perturbation analysis below.

Note that the magnetic anisotropy of the Co4 layer at the *vacuum* side remains almost unchanged across all the structures.

In Fig. 13, we show that Co in a Co/Al bilayer indeed acquires a large PMA [see Figs. 13(a) and 13(d)], but this is a purely structural effect due to *in-plane biaxial strain* from the (≈ 14% larger) lattice parameter of Al acting on the ultrathin Co. Interestingly, the effect survives even when the Al is replaced by vacuum [see Figs. 13(b) and 13(e)], as long as the Co structure is kept frozen at its relaxed state before Al removal. In fact, looking at the difference of the cases with vacuum and with Al [see Figs. 13(c) and 13(f)] shows that proximity with Al actually *decreases* the PMA of Co interfacial layers. This is, however, secondary, as we find that the strain-induced PMA enhancement in the bulklike layers is still the dominant effect. Overall, the results predict that Al will strongly enhance the PMA of the ultrathin Co film.

1. Anisotropy of Co/oxide interface from perturbation analysis

In second-order perturbation theory, the magnetic anisotropy energy of atom i can be written as the sum of two spin-conserving and two spin-flip terms [50],

$$E^i_{\mathrm{MCA}} = \Delta E^i_{\downarrow\Rightarrow\downarrow} + \Delta E^i_{\uparrow\Rightarrow\uparrow} - \Delta E^i_{\uparrow\Rightarrow\downarrow} - \Delta E^i_{\downarrow\Rightarrow\uparrow}, \quad \text{(H1)}$$

each of them being a sum of virtual excitations $\mu \to \mu' \to \lambda' \to \lambda$ of occupied states μ, λ, and unoccupied states

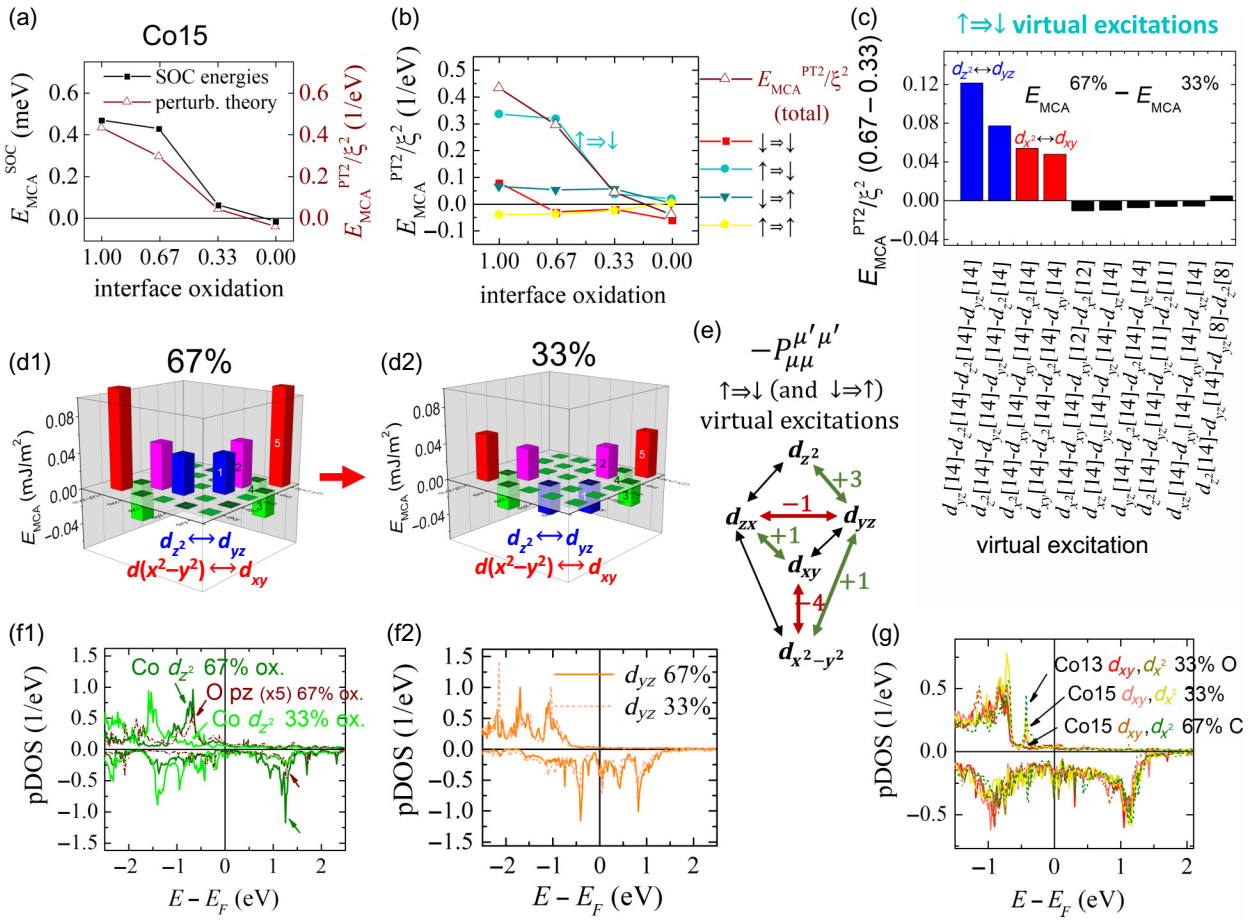

FIG. 14. Perturbation theory analysis of the magnetic anisotropy at the Co/O interface. (a) Perturbation theory predicts the trend in the calculated magnetic anisotropy. (b) It can be resolved into the four spin-interaction contributions. The ↑⇒↓ contribution is dominant. (c) The ↑⇒↓ contribution can be further resolved into orbital interactions. The biggest change between the 67% and 33% cases comes from $d_{z^2} \leftrightarrow d_{yz}$ and $d_{xy} \leftrightarrow d_{x^2-y^2}$. (d1),(d2) This is confirmed by the SOC-associated energies. (e) The $-P^{\mu'\mu'}_{\mu\mu}$ coefficients from Eq. (H2); the negative sign is due to spin flip [see Eq. (H1)], and μ and μ' correspond to two distinct d orbitals. The contribution to PMA from ↑⇒↓ $d_{z^2} \leftrightarrow d_{yz}$ is positive (+3), while that from $d_{xy} \leftrightarrow d_{x^2-y^2}$ is negative (−4; in-plane anisotropy). (f1) The d_{z^2} states indeed appear near the Fermi level due to hybridization with oxygen's p_z states, while (f2) the d_{yz} states remain unchanged by oxidation. (g) The $(d_{xy}, d_{x^2-y^2})$ states appear near the Fermi level at low oxidation due to in-plane hybridization with neighboring cobalt atoms.

$\mu', \lambda',$

$$\Delta E^{i}_{\sigma\Rightarrow\sigma'} = -\xi_i \sum_{\mu,\lambda,\mu',\lambda'} P^{\mu'\lambda'}_{\mu\lambda} \times \sum_{j} \xi_j G^{\mu'\lambda'}_{\mu\lambda}(\sigma,\sigma';i,j), \tag{H2}$$

where ξ_i is the spin-orbit coupling constant of atom i, $P^{\mu'\lambda'}_{\mu\lambda}$ indicates a prefactor coefficient, and $G^{\mu'\lambda'}_{\mu\lambda}$ is the joint density of states.

The PMA decrease with oxygen removal is reproduced by second-order perturbation theory analysis [see Fig. 14(a)] and it comes from the majority ⇒ minority contribution [see Fig. 14(b)], in particular from changes in the $d_{z2} \leftrightarrow d_{yz}$ and $d_{xy} \leftrightarrow d_{x^2-y^2}$ interaction [see Fig. 14(c)], which is also the dominant change in the *ab initio* spin-orbit coupling energy [see Fig. 14(d1,d2)].

The $d_{z2} \leftrightarrow d_{yz}$ majority ⇒ minority interaction gives rise to PMA [see Fig. 14(e)] and is strongly present for oxidized cobalt, where the d_{z2} ↑ orbitals appear near the Fermi level due to hybridization with O p_z [see Fig. 14(f1)]. The d_{z2} states get pushed lower below the Fermi level after oxygen removal, which weakens this positive contribution. The d_{yz} states are not affected by the presence of oxygen [see Fig. 14(f2)].

The $d_{xy} \leftrightarrow d_{x^2-y^2}$ majority ⇒ minority interaction gives rise to in-plane anisotropy [negative coefficient in Fig. 14(e)] and appears in cobalt due to hybridization with neighboring cobalt atoms when oxygen is removed. The peak in the partial DOS of d_{xy} and $d_{x^2-y^2}$ at low interface oxidation is clear from Fig. 14(g). This is a smaller effect that reduces the PMA when removing oxygen.

2. Anisotropy of strained hcp Co from perturbation analysis

The PMA increase with in-plane biaxial strain of the four-monolayer hcp Co slab from Fig. 5(b) is also reproduced by second-order perturbation theory analysis

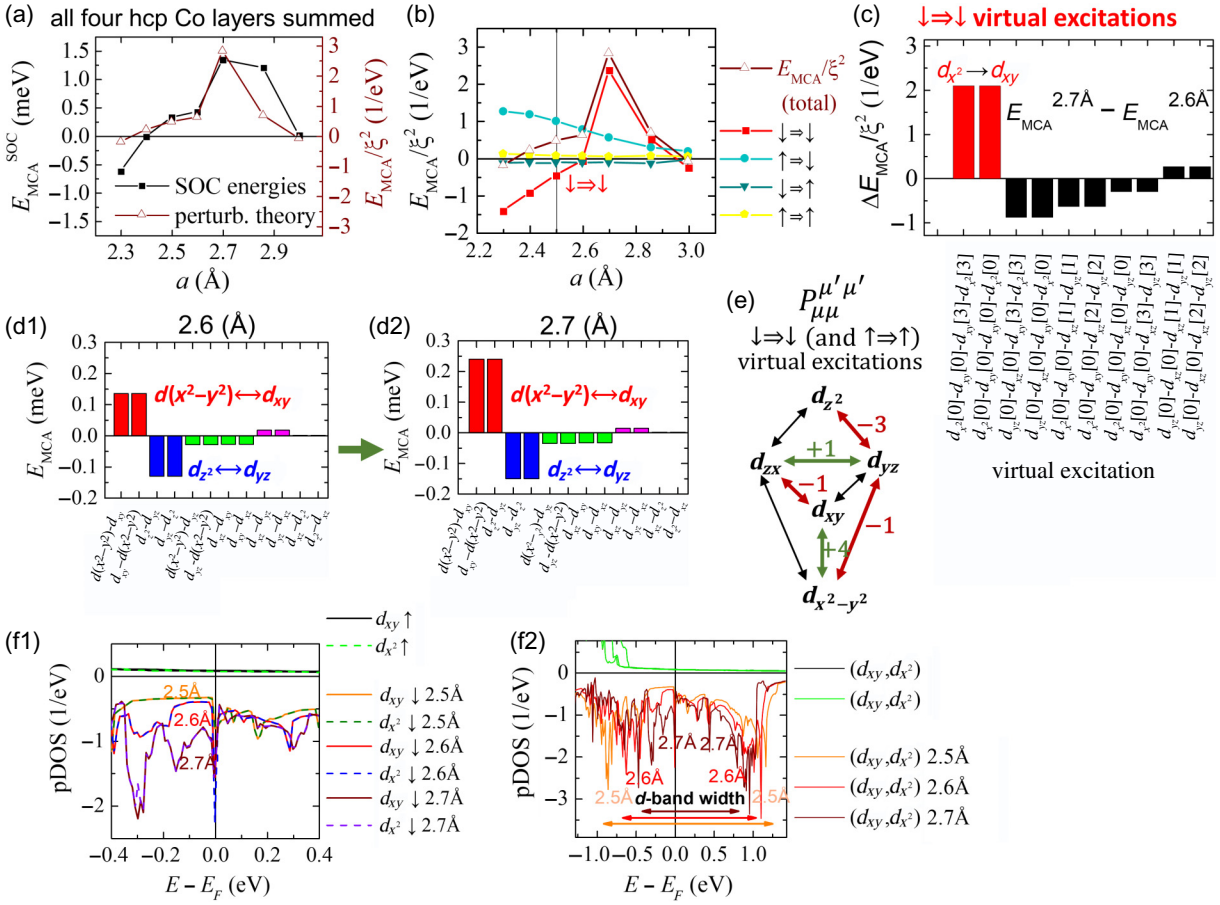

FIG. 15. The perturbation theory analysis of the magnetic anisotropy in in-plane biaxially strained hcp Co. (a) Perturbation theory predicts the trend in the calculated magnetic anisotropy. (b) It can be resolved into the four spin-interaction contributions. The ↓⇒↓ contribution is dominant. (c) The ↓⇒↓ contribution can be further resolved into orbital interactions. The biggest change between the $a = 2.6$ Å and $a = 2.7$ Å cases comes from $d_{xy} \leftrightarrow d_{x^2-y^2}$. (d1),(d2) This is confirmed by the SOC-associated energies. (e) The $P^{\mu'\mu'}_{\mu\mu}$ coefficients from Eq. (H2). The contribution to PMA from ↓⇒↓ $d_{xy} \leftrightarrow d_{x^2-y^2}$ is positive (+4). (f1) The $(d_{xy}, d_{x^2-y^2})$ minority states appear near the Fermi level as (f2) the width of the $(d_{xy}, d_{x^2-y^2})$ band reduces since the cobalt atoms get further apart.

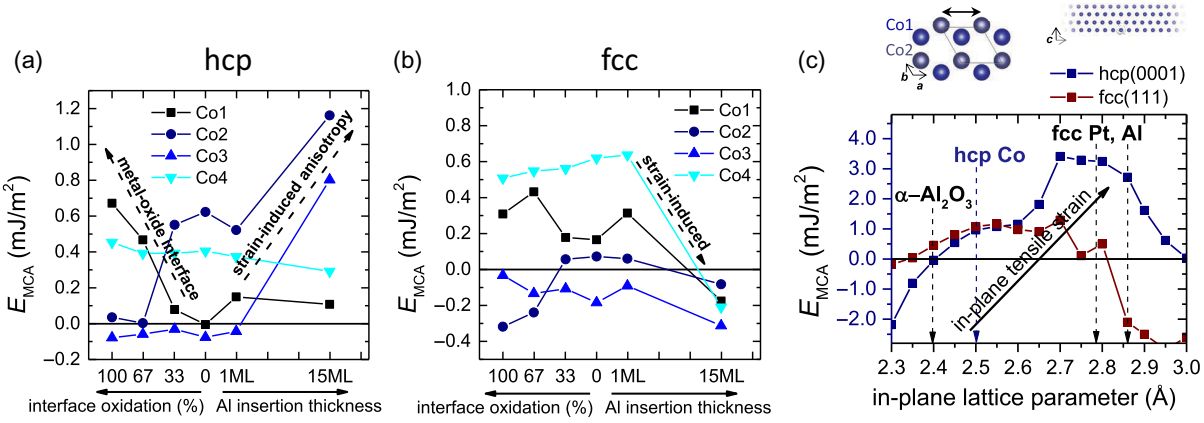

FIG. 16. Magnetocrystalline anisotropy energy of hcp(0001) and fcc(111) cobalt calculated from *ab initio* total energies in Co layers (Co1 is at the interface): (a),(b) as a function of interfacial oxygen content for the six structures from Fig. 10 with (a) hcp(0001) and (b) fcc(111) Co; and (c) for a varying in-plane lattice parameter. The vertical dashed lines in panel (c) indicate in-plane lattice parameters.

[Fig. 15(a)] and comes from the minority ⇒ minority interaction [Fig. 15(b)], in particular changes in the $d_{xy} \leftrightarrow d_{x^2-y^2}$ interaction [Fig. 15(c)], which is also the dominant change in the *ab initio* spin-orbit coupling energy [Fig. 15(d1,d2)].

The $d_{xy} \leftrightarrow d_{x^2-y^2}$ minority ⇒ minority interaction gives rise to PMA [Fig. 15(e)] and is enhanced in biaxially strained hcp Co where the $(d_{xy}, d_{x^2-y^2})$ orbitals appear near the Fermi level [Fig. 15(f1)]. This is because the $(d_{xy}, d_{x^2-y^2})$ band gets narrower [Fig. 15(f2)] due to the reduced hopping between the neighboring in-plane cobalt atoms, as they get further apart due to strain. The increase in the Fermi-level DOS of $(d_{xy}, d_{x^2-y^2})$ minority states is thus at the origin of the strain-induced magnetic anisotropy of hcp Co.

APPENDIX I: hcp(0001) AND fcc(111) COBALT

1. *Ab initio* results

The stable form of Co below 400 °C is hcp(0001) with its ABAB stacking, corresponding also to the ϵ phase identified in our XRD analysis (see below). For sputtered samples, the growth is hcp [52]. In order to confirm the robustness of the results, we have recalculated the results

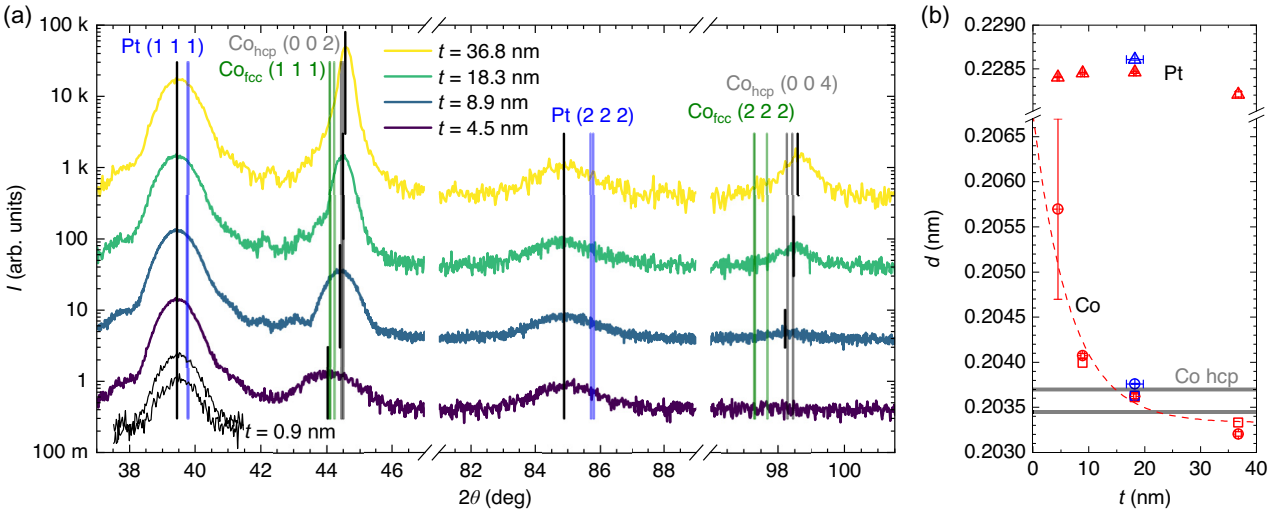

FIG. 17. X-ray diffraction of thick Co films. (a) Symmetric θ–2θ scans of Ta(5 nm)/Pt(8 nm)/Co(t)/Al(5 nm) films in Bragg-Brentano geometry using a Cu $K\alpha$ source. Black lines are estimated positions of the experimental peaks; colored lines are reference positions from the (Powder Diffraction File) PDF-5+ database (00-004-0802, 00-072-0455, 01-071-4239, 01-071-4651, 01-077-7456, 01-080-6668, and 01-090-5299). The Pt(111) peaks of Al 0.7-nm and 1.0-nm samples from the main text are shown (bottom left) in black with the label $t = 0.9$ nm. (b) Estimated out-of-plane parameters from the diffractograms in panel (a). The red circles and red squares correspond to the (002) and (004) Co hcp peaks, respectively. The triangles correspond to the Pt(111). The blue data points were acquired on another machine with only the $K\alpha 1$ line (0.15406 nm). The interplane distance for the red data points is estimated using a mean wavelength of 0.1542 nm. The red dashed line is an exponential decay used as a guide to the eye.

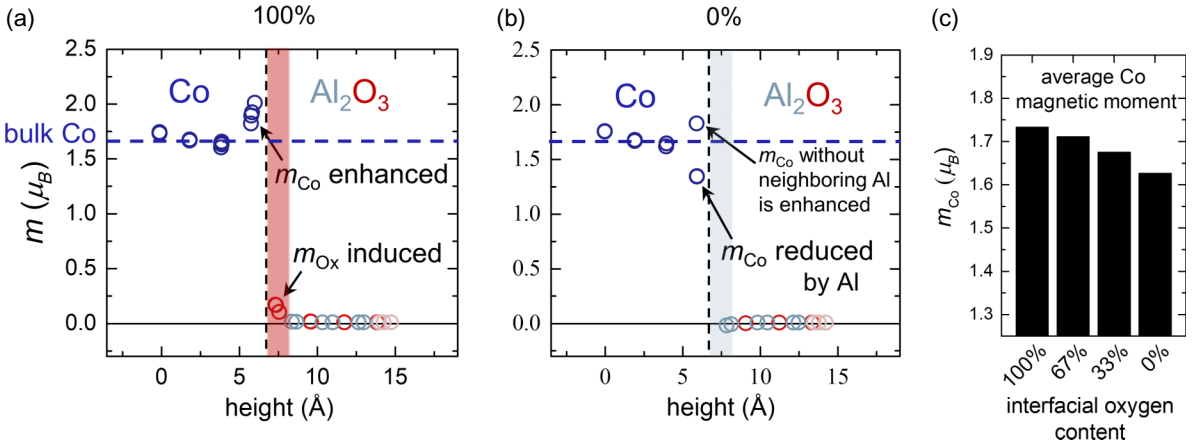

FIG. 18. The spin magnetic moment of $Co/Al/Al_2O_3$ with (a) 100% and (b) 0% interface oxidation, resolved for all atoms from the crystal structure (Fig. 10). (c) The average Co spin magnetic moment as a function of Co/AlO interface oxidation.

of Fig. 5, swapping hcp Co for its fcc phase. The results are shown side-by-side in Figs. 16(a) and 16(b). It is clear that magnetic anisotropy enhancement with tensile strain does not occur for the fcc phase. On the contrary, tensile strain seems to strongly *decrease* the PMA in fcc Co, and this is further emphasized in Fig. 16(c), where the in-plane lattice parameter was varied for a four-monolayer Co slab in vacuum, the same as in Fig. 5(b), comparing here the hcp and fcc Co. An interesting conclusion can be drawn from Fig. 16(c), namely that a structural transformation from the (metastable) fcc phase to the (stable) hcp phase (e.g., upon annealing) will lead to a large anisotropy enhancement, provided that cobalt is strained by several percent (away from its equilibrium lattice parameter of ≈ 2.5 Å.

2. X-ray measurements

Previous reports of Co grown by sputtering suggest Co growth in the expected ϵ phase, i.e., hcp (see Ref. [52] and references therein). Here, we compare our data with those published by Patel *et al.* [52], their article dedicated to the proof that Co grows hcp over Pt.

Experimentally, using our laboratory x rays, it is not possible to detect the diffracted signal from four atomic layers. Therefore, we studied the evolution of the diffraction peaks of thicker Co films, ranging from 4.5 to 37 nm. As shown in Fig. 17, the Pt(111) peak stays at a constant position, slightly lower than expected due to growth-induced strain (ion-peening effect), while the Co peak associated with the (002ℓ) planes of the hcp structure shift considerably with the Co thickness, suggesting a rapid relaxation toward the bulk parameter. All these results are remarkably consistent with those reported in Fig. 2 of Patel *et al.* [52]. Such strain relaxation is not surprising, as the Co layer cannot sustain a 11.4% tensile strain over a few nanometers. With such a strain level, crystalline growth (at the grain level) is still possible, but defects are generated in the first few layers (see, e.g., the review by Narayan [53]). We could also observe a peak corresponding to the Co(101) planes of the hcp phase (at $2\theta = 47.39°$, $\chi = 61°$), which does not exist for the fcc phase.

APPENDIX J: SPIN AND ORBITAL MAGNETIC MOMENTS

The *ab initio* spin magnetic moment of cobalt shows an enhancement by the oxygen interface, while both the spin and orbital magnetic moments are reduced at the aluminum interface. (An increase of the magnetic moment due to an oxygen interface can also be observed in *ab initio* calculations with Fe [54].)

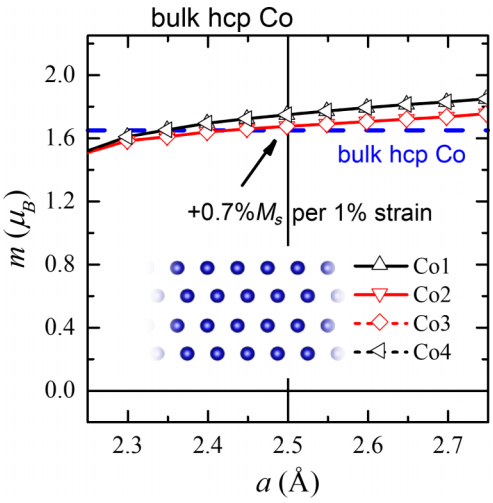

FIG. 19. Strain slightly increases the spin magnetic moment, but this is secondary to changes in the interfacial Co magnetic moment due to the Co/O versus Co/Al interface.

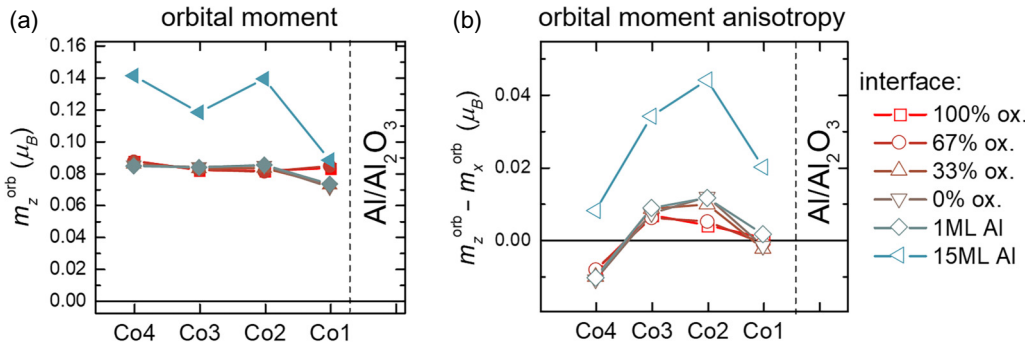

FIG. 20. (a) Orbital magnetization and (b) its anisotropy in $Co/Al/Al_2O_3$. Large variation is observed at the interfacial Co1 in all the structures. For the Co/Al(15 ML) structure in particular, large orbital moments are observed in all the four Co layers, linked to the strain-induced magnetic anisotropy detailed in Appendix H.

1. Spin magnetization

The spin magnetic moment of the interfacial Co layer is enhanced by $\approx 15\%$ by the proximity with oxygen, and a small magnetic moment ($\approx 0.1\ \mu_B$) is also induced in the interfacial oxygen itself [see Fig. 18(a)]. In contrast, the spin magnetic moment is reduced by $\approx 20\%$ at the Al interface [see Fig. 18(b)]. The total magnetization therefore decreases when replacing interfacial oxygen with aluminum due to all of these effects synergically. Overall, we find a decrease of the magnetization when removing oxygen from the interface, as shown in Fig. 18(c), in agreement with the experimental observations.

Increase of magnetic moment. A positive strain on Co is expected during an Al insertion due to their lattice mismatch. In Fig. 19, we show that the spin magnetization monotonically increases for such larger lattice parameters, at a rate about $+0.7\%$ per $+1\%$ in-plane biaxial strain. This slight increase in magnetization is, however, secondary compared to the large *decrease* due to the $Co/O \rightarrow Co/Al$ transition described above.

2. Orbital magnetization

Even though the orbital magnetization is typically small in $3d$ metals, its anisotropy $\Delta\mu_{\rm orb} \equiv \mu_\perp - \mu_\parallel$ is very relevant, because it is anticipated to be proportional to the magnetocrystalline anisotropy energy,

$$\Delta E_{\rm MCA} = \frac{\xi}{S_{\rm unit\ cell}} \frac{\Delta\mu_{\rm orb}}{4\mu_B}, \tag{J1}$$

in the picture of the Bruno's model, where the SOC constant ξ binds the spin and orbital magnetic moments.

For the interfacial Co1, both the orbital magnetic moment and its anisotropy decrease compared to values for the other three Co layers, as shown in Figs. 20(a) and 20(b). The same trend is found in the $E_{\rm MCA}$ results of Fig. 12, confirming Bruno's model picture in this system. Note that for Co/Al(15 ML) we predict a much larger orbital magnetic moment and its anisotropy compared to the other structures. This is also reflected in the magnetocrystalline anisotropy (Fig. 12).

[1] A. Soumyanarayanan, N. Reyren, A. Fert, and C. Panagopoulos, Emergent phenomena induced by spin–orbit coupling at surfaces and interfaces, Nature **539**, 509 (2016).

[2] B. Dieny and M. Chshiev, Perpendicular magnetic anisotropy at transition metal/oxide interfaces and applications, Rev. Mod. Phys. **89**, 025008 (2017).

[3] A. Thiaville, S. Rohart, Émilie Jué, V. Cros, and A. Fert, Dynamics of Dzyaloshinskii domain walls in ultrathin magnetic films, Europhys. Lett. **100**, 57002 (2012).

[4] A. Fert, M. Chshiev, A. Thiaville, and H. Yang, From early theories of Dzyaloshinskii–Moriya interactions in metallic systems to today's novel roads, J. Phys. Soc. Jpn. **92**, 081001 (2023).

[5] I. M. Miron, K. Garello, G. Gaudin, P.-J. Zermatten, M. V. Costache, S. Auffret, S. Bandiera, B. Rodmacq, A. Schuhl, and P. Gambardella, Perpendicular switching of a single ferromagnetic layer induced by in-plane current injection, Nature **476**, 189 (2011).

[6] S. Krishnia, Y. Sassi, F. Ajejas, N. Sebe, N. Reyren, S. Collin, T. Denneulin, A. Kovács, R. E. Dunin-Borkowski, A. Fert, J.-M. George, V. Cros, and H. Jaffrès, Large interfacial Rashba interaction generating strong spin–orbit torques in atomically thin metallic heterostructures, Nano Lett. **23**, 6785 (2023).

[7] N. Nakajima, T. Koide, T. Shidara, H. Miyauchi, H. Fukutani, A. Fujimori, K. Iio, T. Katayama, M. Nývlt, and Y. Suzuki, Perpendicular magnetic anisotropy caused by interfacial hybridization via enhanced orbital moment in Co/Pt multilayers: Magnetic circular x-ray dichroism study, Phys. Rev. Lett. **81**, 5229 (1998).

[8] P. F. Carcia, A. D. Meinhaldt, and A. Suna, Perpendicular magnetic anisotropy in Pd/Co thin film layered structures, Appl. Phys. Lett. **47**, 178 (1985).

[9] D. Weller, Y. Wu, J. Stöhr, M. G. Samant, B. D. Hermsmeier, and C. Chappert, Orbital magnetic moments of Co in multilayers with perpendicular magnetic anisotropy, Phys. Rev. B **49**, 12888 (1994).

[10] B. Rodmacq, S. Auffret, B. Dieny, S. Monso, and P. Boyer, Crossovers from in-plane to perpendicular anisotropy in magnetic tunnel junctions as a function of the barrier degree of oxidation, J. Appl. Phys. **93**, 7513 (2003).

[11] A. Manchon, C. Ducruet, L. Lombard, S. Auffret, B. Rodmacq, B. Dieny, S. Pizzini, J. Vogel, V. Uhlíř, M. Hochstrasser, and G. Panaccione, Analysis of oxygen induced anisotropy crossover in Pt/Co/*M*Ox trilayers, J. Appl. Phys. **104**, 043914 (2008).

[12] Y. Dahmane, C. Arm, S. Auffret, U. Ebels, B. Rodmacq, and B. Dieny, Oscillatory behavior of perpendicular magnetic anisotropy in Pt/Co/Al(O_x) films as a function of Al thickness, Appl. Phys. Lett. **95**, 222514 (2009).

[13] S. Monso, B. Rodmacq, S. Auffret, G. Casali, F. Fettar, B. Gilles, B. Dieny, and P. Boyer, Crossover from in-plane to perpendicular anisotropy in Pt/CoFe/AlO_x sandwiches as a function of Al oxidation: A very accurate control of the oxidation of tunnel barriers, Appl. Phys. Lett. **80**, 4157 (2002).

[14] C. Balan, J. Fischer, C. Gueneau, A. Fassatoui, J.-P. Rueff, D. Ceolin, M. De-Santis, J. Vogel, L. Ranno, H. Béa, and S. Pizzini, Using hard-x-ray photoelectron spectroscopy to measure the oxidation state of gated Co/Al_x interfaces, Phys. Rev. Appl. **21**, 064023 (2024).

[15] H. X. Yang, M. Chshiev, B. Dieny, J. H. Lee, A. Manchon, and K. H. Shin, First-principles investigation of the very large perpendicular magnetic anisotropy at Fe|MgO and Co|MgO interfaces, Phys. Rev. B **84**, 054401 (2011).

[16] S. Peng, M. Wang, H. Yang, L. Zeng, J. Nan, J. Zhou, Y. Zhang, A. Hallal, M. Chshiev, K. L. Wang, Q. Zhang, and W. Zhao, Origin of interfacial perpendicular magnetic anisotropy in MgO/CoFe/metallic capping layer structures, Sci. Rep. **5**, 18173 (2015).

[17] N. Rougemaille, A. T. N'Diaye, J. Coraux, C. Vo-Van, O. Fruchart, and A. K. Schmid, Perpendicular magnetic anisotropy of cobalt films intercalated under graphene, Appl. Phys. Lett. **101**, 142403 (2012).

[18] H. Yang, A. D. Vu, A. Hallal, N. Rougemaille, J. Coraux, G. Chen, A. K. Schmid, and M. Chshiev, Anatomy and giant enhancement of the perpendicular magnetic anisotropy of cobalt–graphene heterostructures, Nano Lett. **16**, 145 (2016).

[19] H. Yang, G. Chen, A. A. C. Cotta, A. T. N'Diaye, S. A. Nikolaev, E. A. Soares, W. A. A. Macedo, K. Liu, A. K. Schmid, A. Fert, and M. Chshiev, Significant Dzyaloshinskii–Moriya interaction at graphene–ferromagnet interfaces due to the Rashba effect, Nat. Mater. **17**, 605 (2018).

[20] A. Hallal, J. Liang, F. Ibrahim, H. Yang, A. Fert, and M. Chshiev, Rashba-type Dzyaloshinskii–Moriya interaction, perpendicular magnetic anisotropy, and skyrmion states at 2D materials/Co interfaces, Nano Lett. **21**, 7138 (2021).

[21] B. El-Kerdi, A. Thiaville, S. Rohart, S. Panigrahy, N. Brás, J. Sampaio, and A. Mougin, Evidence of strong Dzyaloshinskii–Moriya interaction at the cobalt/hexagonal boron nitride interface, Nano Lett. **23**, 3202 (2023).

[22] S. A. Nikolaev, M. Chshiev, F. Ibrahim, S. Krishnia, N. Sebe, J. M. George, V. Cros, H. Jaffrès, and A. Fert, Large chiral orbital texture and orbital Edelstein effect in Co/Al heterostructure, Nano Lett. **24**, 13465 (2024).

[23] A. Fert, N. Reyren, and V. Cros, Magnetic skyrmions: Advances in physics and potential applications, Nat. Rev. Mater. **2**, 17031 (2017).

[24] M. Belmeguenai, J.-P. Adam, Y. Roussigné, S. Eimer, T. Devolder, J.-V. Kim, S. M. Cherif, A. Stashkevich, and A. Thiaville, Interfacial Dzyaloshinskii-Moriya interaction in perpendicularly magnetized Pt/Co/AlO_x ultrathin films measured by Brillouin light spectroscopy, Phys. Rev. B **91**, 180405 (2015).

[25] N.-H. Kim, D.-S. Han, J. Jung, K. Park, H. J. M. Swagten, J.-S. Kim, and C.-Y. You, Dependence of interfacial Dzyaloshinskii–Moriya interaction and perpendicular magnetic anisotropy on the thickness of the heavy-metal layer, Appl. Phys. Express **10**, 103003 (2017).

[26] R. Lo Conte, G. V. Karnad, E. Martinez, K. Lee, N.-H. Kim, D.-S. Han, J.-S. Kim, S. Prenzel, T. Schulz, C.-Y. You, H. J. M. Swagten, and M. Kläui, Ferromagnetic layer thickness dependence of the Dzyaloshinskii-Moriya interaction and spin-orbit torques in Pt/Co/AlO_x, AIP Adv. **7**, 065317 (2017).

[27] X. Ma, G. Yu, C. Tang, X. Li, C. He, J. Shi, K. L. Wang, and X. Li, Interfacial Dzyaloshinskii-Moriya interaction: Effect of 5*d* band filling and correlation with spin mixing conductance, Phys. Rev. Lett. **120**, 157204 (2018).

[28] M. Kuepferling, A. Casiraghi, G. Soares, G. Durin, F. Garcia-Sanchez, L. Chen, C. H. Back, C. H. Marrows, S. Tacchi, and G. Carlotti, Measuring interfacial Dzyaloshinskii-Moriya interaction in ultrathin magnetic films, Rev. Mod. Phys. **95**, 015003 (2023).

[29] F. Ajejas, Y. Sassi, W. Legrand, S. Collin, J. Peña Garcia, A. Thiaville, S. Pizzini, N. Reyren, V. Cros, and A. Fert, Interfacial potential gradient modulates Dzyaloshinskii-Moriya interaction in Pt/Co/metal multilayers, Phys. Rev. Mater. **6**, L071401 (2022).

[30] V. M. Parakkat, K. R. Ganesh, and P. S. Anil Kumar, Tailoring Curie temperature and magnetic anisotropy in ultrathin Pt/Co/Pt films, AIP Adv. **6**, 056118 (2016).

[31] P. Carcia and W. Zeper, Sputtered Pt/Co multilayers for magneto-optical recording, IEEE Trans. Magn. **26**, 1703 (1990).

[32] B. Zimmermann, W. Legrand, D. Maccariello, N. Reyren, V. Cros, S. Blügel, and A. Fert, Dzyaloshinskii-Moriya interaction at disordered interfaces from *ab initio* theory: Robustness against intermixing and tunability through dusting, Appl. Phys. Lett. **113**, 232403 (2018).

[33] C. T. Chen, Y. U. Idzerda, H.-J. Lin, N. V. Smith, G. Meigs, E. Chaban, G. H. Ho, E. Pellegrin, and F. Sette, Experimental confirmation of the x-ray magnetic circular dichroism sum rules for iron and cobalt, Phys. Rev. Lett. **75**, 152 (1995).

[34] Y. Wang and J. P. Perdew, Correlation hole of the spin-polarized electron gas, with exact small-wave-vector and high-density scaling, Phys. Rev. B **44**, 13298 (1991).

[35] J. P. Perdew, K. Burke, and M. Ernzerhof, Generalized gradient approximation made simple, Phys. Rev. Lett. **77**, 3865 (1996).

[36] G. Kresse and J. Hafner, *Ab initio* molecular dynamics for liquid metals, Phys. Rev. B **47**, 558 (1993).

[37] G. Kresse and J. Furthmüller, Efficiency of *ab-initio* total energy calculations for metals and semiconductors using a plane-wave basis set, Comput. Mater. Sci. **6**, 15 (1996).

[38] G. Kresse and J. Furthmüller, Efficient iterative schemes for *ab initio* total-energy calculations using a plane-wave basis set, Phys. Rev. B **54**, 11169 (1996).

[39] G. Kresse and D. Joubert, From ultrasoft pseudopotentials to the projector augmented-wave method, Phys. Rev. B **59**, 1758 (1999).

[40] A. Belabbes, G. Bihlmayer, S. Blügel, and A. Manchon, Oxygen-enabled control of Dzyaloshinskii-Moriya interaction in ultra-thin magnetic films, Sci. Rep. **6**, 24634 (2016).

[41] H. Yang, O. Boulle, V. Cros, A. Fert, and M. Chshiev, Controlling Dzyaloshinskii-Moriya interaction via chirality dependent atomic-layer stacking, insulator capping and electric field, Sci. Rep. **8**, 12356 (2018).

[42] A. Hallal, B. Dieny, and M. Chshiev, Impurity-induced enhancement of perpendicular magnetic anisotropy in Fe/MgO tunnel junctions, Phys. Rev. B **90**, 064422 (2014).

[43] T. da Câmara Santa Clara Gomes, T. Bhatnagar-Schöffmann, S. Krishnia, Y. Sassi, D. Sanz-Hernández, N. Reyren, M.-B. Martin, F. Brunnett, S. Collin, F. Godel, S. Ono, D. Querlioz, D. Ravelosona, V. Cros, J. Grollier, P. Seneor, and L. Herrera Diez, Control of the magnetic anisotropy in multirepeat Pt/Co/Al heterostructures using magnetoionic gating, Phys. Rev. Appl. **21**, 024010 (2024).

[44] P. Ohresser, E. Otero, F. Choueikani, K. Chen, S. Stanescu, F. Deschamps, T. Moreno, F. Polack, B. Lagarde, J.-P. Daguerre, F. Marteau, F. Scheurer, L. Joly, J.-P. Kappler, B. Muller, O. Bunau, and P. Sainctavit, DEIMOS: A beamline dedicated to dichroism measurements in the 350–2500 eV energy range, Rev. Sci. Instrum. **85**, 013106 (2014).

[45] K. Di, V. L. Zhang, H. S. Lim, S. C. Ng, M. H. Kuok, J. Yu, J. Yoon, X. Qiu, and H. Yang, Direct observation of the Dzyaloshinskii-Moriya interaction in a Pt/Co/Ni film, Phys. Rev. Lett. **114**, 047201 (2015).

[46] O. Boulle, J. Vogel, H. Yang, S. Pizzini, D. de Souza Chaves, A. Locatelli, T. O. Menteş, A. Sala, L. D. Buda-Prejbeanu, O. Klein, M. Belmeguenai, Y. Roussigné, A. Stashkevich, S. M. Chérif, L. Aballe, M. Foerster, M. Chshiev, S. Auffret, I. M. Miron, and G. Gaudin, Room-temperature chiral magnetic skyrmions in ultrathin magnetic nanostructures, Nat. Nanotechnol. **11**, 449 (2016).

[47] K. Momma and F. Izumi, *VESTA 3* for three-dimensional visualization of crystal, volumetric and morphology data, J. Appl. Crystallogr. **44**, 1272 (2011).

[48] H. Yang, A. Thiaville, S. Rohart, A. Fert, and M. Chshiev, Anatomy of Dzyaloshinskii-Moriya interaction at Co/Pt interfaces, Phys. Rev. Lett. **115**, 267210 (2015).

[49] P. Bruno, Tight-binding approach to the orbital magnetic moment and magnetocrystalline anisotropy of transition-metal monolayers, Phys. Rev. B **39**, 865 (1989).

[50] Y. Miura, S. Ozaki, Y. Kuwahara, M. Tsujikawa, K. Abe, and M. Shirai, The origin of perpendicular magnetocrystalline anisotropy in $L1_0$-FeNi under tetragonal distortion, J. Phys.: Condens. Matter **25**, 106005 (2013).

[51] L. Vojáček, F. Ibrahim, A. Hallal, B. Dieny, and M. Chshiev, Giant perpendicular magnetic anisotropy enhancement in MgO-based magnetic tunnel junction by using Co/Fe composite layer, Phys. Rev. Appl. **15**, 024017 (2021).

[52] G. Patel, F. Ganss, R. Salikhov, S. Stienen, L. Fallarino, R. Ehrler, R. A. Gallardo, O. Hellwig, K. Lenz, and J. Lindner, Structural and magnetic properties of thin cobalt films with mixed hcp and fcc phases, Phys. Rev. B **108**, 184429 (2023).

[53] J. Narayan, Recent progress in thin film epitaxy across the misfit scale (2011 Acta Gold Medal paper), Acta Mater. **61**, 2703 (2013).

[54] H. X. Yang, M. Chshiev, B. Dieny, J. H. Lee, A. Manchon, and K. H. Shin, First-principles investigation of the very large perpendicular magnetic anisotropy at Fe|MgO and Co|MgO interfaces, Phys. Rev. B **84**, 054401 (2011).